



AIAA 2004-3474

**Inviscid Models of
the Classic Hybrid Rocket**

J. Majdalani and A. B. Vyas
Advanced Theoretical Research Center
University of Tennessee Space Institute

Propulsion Conference and Exhibit

11–14 July 2004
Fort Lauderdale, FL

Inviscid Models of the Classic Hybrid Rocket

Joseph Majdalani* and Anand B. Vyas†
University of Tennessee Space Institute, Tullahoma, TN 37388

In this work, we derive two analytical solutions that mimic the bulk gas motion corresponding to the classic full-length, cylindrical hybrid rocket engine with circular bore. Our approach is based on steady, axisymmetric, incompressible, and inviscid flow conditions. Two exact solutions are presented starting from Euler's equations. The first is rotational, assumes normal sidewall mass addition, and employs a harmonic injection profile at the head end wall. The second is irrotational but allows uniform head end injection. The resulting formulations enable us to model the streamtubes observed in conventional hybrid engines in which the parallel motion of gaseous oxidizer is coupled with the cross-streamwise (i.e., sidewall) addition of solid fuel. Furthermore, estimates for pressure, velocity and vorticity distributions in the simulated engine are provided in closed form. The idealized hybrid engine is modeled as a porous circular-port chamber with head end injection. The mathematical treatment is based on a standard similarity approach that is tailored to accept either sinusoidal or uniform injection at the head end.

Nomenclature

- a = chamber radius
 p = normalized pressure, $\bar{p}/(\rho U_w^2)$
 Re = wall injection Reynolds number, $U_w a / \nu$
 r = normalized radial coordinate, \bar{r} / a
 \mathbf{u} = normalized velocity (\bar{u}_r, \bar{u}_z)/ U_w
 U_0 = maximum head end injection velocity, $\bar{u}_z(0, 0)$
 u_0 = normalized head end injection velocity, U_0 / U_w
 u_h = head end injection constant, $u_0 / \pi = U_0 / (\pi U_w)$
 U_w = wall injection velocity, $-\bar{u}_r(a, \bar{z})$
 z = normalized axial coordinate, \bar{z} / a
- ν = kinematic viscosity, μ / ρ
 ρ = density
 $\boldsymbol{\Omega}$ = vorticity, $\nabla \times \mathbf{u}$

Subscripts and Symbols

- h = property at the head end
 r = radial component or partial derivative
 w = property at the sidewall
 z = axial component or partial derivative
 = overbars denote dimensional variables

*Jack D. Whitfield Professor of High Speed Flows,
 Department of Mechanical, Aerospace and Biomedical
 Engineering. Member AIAA.

†Research Scientist and former Instructor, Marquette
 University, Department of Mechanical and Industrial
 Engineering. Member AIAA.

I. Introduction

WHEN considering different methods of propulsion, it must be borne in mind that there is an overall hierarchy of engines depending on the application at hand. Among rocket engines there are two general types, electrical and chemical. While electrical motors are efficient and fuel economical, they provide such little thrust that they are primarily employed in supra-orbital missions. For heavy payload launches, one resorts to chemical rockets.

It is well known that, in chemical rockets, at least two substances, a fuel and an oxidizer, must be mixed in a certain way depending on the propellant type and category. The chemical energy associated with combining these two substances is transferred to the gaseous products which, in turn, are expanded through a nozzle; the expansion process produces the desired thrust for the attached vehicle. Three options are available depending on mission requirements; these are a) solid, b) liquid and c) hybrid rocket motors. In this study, the focus is set on an idealized representation of the cylindrical hybrid motor with circular bore.

To review and compare differences, liquid rockets utilize liquid fuel and oxidizer stored in separate tanks, except in the case of a monopropellant. By either pressure feeding or mechanically pumping the propellants from their tanks, they are guided into a mixing chamber where they are consummated. Liquid rocket engines provide high thrust capability and can be throttled at will. Additionally, they tend to be the most efficient of high-thrust engines. Their main drawback is their complexity owing to their multiple components,

specifically, to their stop-valves, pressure regulators, injectors, baffles, turbopump machinery and other plumbing accessories. Furthermore, in the interest of reliability, the need for system redundancies on most components can claim excessive cost and weight penalties.

The bulk gas motion in a liquid rocket engine is often described using computational fluid dynamics (CFD). In theoretical analyses, a uniform flow is generally assumed for the streamtube motion that the gases undergo soon after injection and combustion.

Solid rocket motors (SRMs) are somewhat different, having a specific set of advantages and drawbacks. In SRMs, the fuel and oxidizer are chemically premixed to form the solid propellant grain. By simply igniting this rubbery or soap-like substance, the oxidizer and fuel in the solid matrix react to produce the high-energy propulsive gases. A variety of designs for the central burning port are available for producing the desired thrust performance. SRMs are simple to build and operate. On the down side, they are less efficient fuel burners and cannot be throttled. They are more hazardous to handle and possess a limited shelf life due to degradation with aging.

In 1966, a simple analytical solution was proposed by Culick¹ for describing the mean gaseous motion in SRMs. His solution was derived under the contingencies of steady, incompressible, rotational, axisymmetric, and inviscid (high Reynolds number) flow. It coincided with Taylor's 1956 solution obtained in a different physical context.² The resulting profile was scrutinized in subsequent studies, including computational,³⁻⁵ experimental,⁵⁻⁷ and recent theoretical investigations;⁸⁻¹⁰ it was found to be quite adequate for modeling the mean flow in a full-length cylindrical motor. To this date, Culick's profile remains at the foundation of several theoretical studies, especially, those concerning combustion instability. Despite its simplicity and abandonment of SRM physicochemistry, it has proven to be quintessential in investigating several performance-related mechanisms that arise in rocket motor internal ballistics.

Hybrid rockets, which combine many of the simplistic features of solids and performance of liquids, seem to offer a compromising solution. In a hybrid, a gaseous or liquid oxidizer (or fuel) is stored in an insulated tank. The fuel grain (or less common oxidizer) is placed inside a thrust chamber extending between an injector faceplate and a nozzle (see Fig. 1). The typically solid grain is hollowed out to produce a combustion port in a fashion similar to that of an SRM. By injecting the oxidizer at a high mass flow rate and pressure into the chamber, reactions are initiated in a thin boundary layer just above the surface of the fuel.

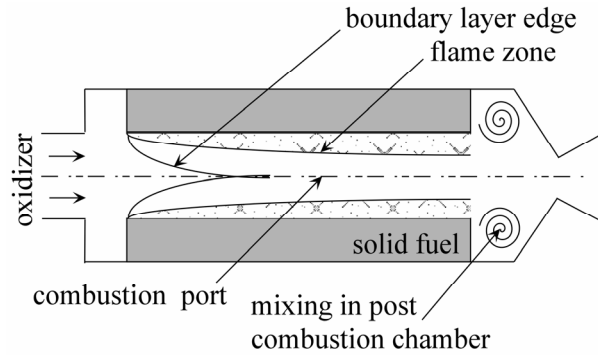


Fig. 1 Schematic of the circular-port hybrid rocket.

The ensuing high combustion temperature helps to sustain solid fuel vaporization. The reaction gases cross the combustion port and are expanded through the nozzle. By metering the oxidizer, the production of exhaust gases and corresponding thrust can be modulated. This gives hybrid rockets throttling and start-stop-restart capabilities.

On the down side, hybrids exhibit lower combustion efficiencies and are susceptible to fluctuations in specific impulse. These setbacks can be chiefly attributed to incomplete mixing in the active combustion zone and the presence of residual slivers at propellant burnout. Fortunately, and despite these relative drawbacks, the specific impulse is only weakly compromised. In practice, conventional hybrids sit on the median between liquid and solid rockets. Their typical performance numbers are available in the open literature: for liquid systems, specific impulse can range between 300 and 400 s; most SRMs operate at an impulse of 200 to 270 s; yet experimental tests put hybrid engines in the 275-350 s range, directly above SRMs.

Several advantages of hybrids are simple to point out. Although they are more complex than SRMs, they compare in performance to liquid systems while requiring half of the usual plumbing. This appreciable reduction in overall engine weight and cost is accompanied by a marked increase in reliability. By comparison with solids, hybrids are safer to produce and store, ecologically less hazardous, and the fuel grain, being inert, is more resilient and, therefore, reliable than solid propellants. By comparison with liquid systems, the partly solid fuel grain of the hybrid grants volumetric loading advantages over the tankage required for liquids. Clearly, hybrid rocket motors can offer several distinct benefits at a reasonable price, especially when technological measures are taken to alleviate their combustion inefficiencies and boost their performance figures. It is in light of these prospects that dedicated teams have been formed at several research

laboratories to design and test increasingly more promising models of hybrid rockets.¹¹⁻¹⁷

In a typical hybrid, an inert solid fuel grain burns in the presence of a gaseous or liquid oxidizer. The resulting diffusion flame resembles that of a household candle: As the hot combustion gases cause a thin layer of the fuel to pyrolyze and vaporize, the oxidizer and fuel particles react along the exposed port areas in several layers or zones of decreasing fuel concentration. This process is illustrated in Fig. 2 where stacked layers of decreasing fuel fraction are shown to separate the oxidizer from the solid fuel grain.

Despite the relative complexity of the fluid structures that lie directly above the fuel surface, the trajectory followed by gases as they are ejected into the chamber can be assumed to be normal to the surface, as in the case of an SRM. In fact, a closed-form analytical approximation, namely, one that will be pursued here, can be used to describe the gas motion corresponding to this idealized representation of a hybrid motor. If slip is allowed at the surface, another solution can be managed, albeit irrotational. In either of the two cases, the interactions within the flame zone must be ignored lest an intractable problem is reached. Instead, the burning surface will be modeled, as in the case of a solid propellant, by assuming a porous surface.¹ The difference here lies in the mass injection across the wall which will be smaller than in the case of a solid propellant. To the authors' knowledge, no analytical solution for the hybrid has yet been advanced. The technique we choose to apply relies on a conventional similarity approach; this will be employed in conjunction with Euler's equations whose application is justified in view of the large Reynolds numbers connected with this problem. The goal will be to construct a steady, inviscid, incompressible mean flow solution for a full-length circular-port hybrid engine.

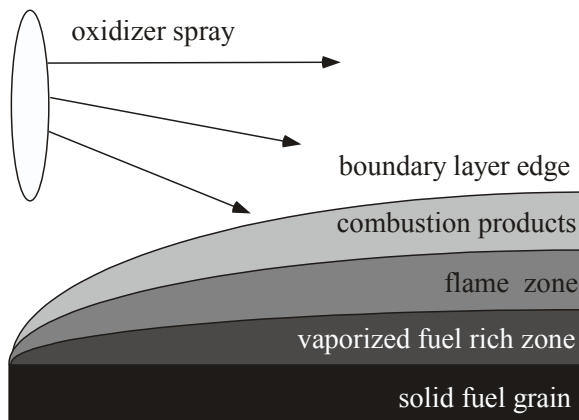


Fig. 2 Decreasing fuel concentration zones above solid surface during hybrid grain pyrolysis.

II. Hybrid Model

The hybrid engine can be modeled as a cylindrical chamber of porous length L and radius a with both a permeable head end and a fully open downstream end. The permeable head end permits the injection of a fluid at a prescribed velocity profile. A sketch of the chamber is given in Fig. 3 where \bar{r} and \bar{z} are used to denote the radial and axial coordinates. The field of interest extends from the head end to the nozzle's attachment point at the base of the chamber. Downstream of the base, the flow is accelerated after expanding through a nozzle whose treatment is not of interest here.

At the head end, an oxidizer stream is injected into the chamber at a maximum centerline speed equal to U_0 . This incoming (oxidizer) gas merges with the peripheral flux due to uniform mass addition at the porous sidewall. The sidewall injection velocity U_w is used to capture the solid fuel regression rate. Clearly, U_w can be appreciably smaller than U_0 due to typical rates of fuel pyrolysis. This condition could be exploited in seeking an asymptotic approximation of higher order. The current analysis seeks to capture the essential features of the ensuing flowfield at leading

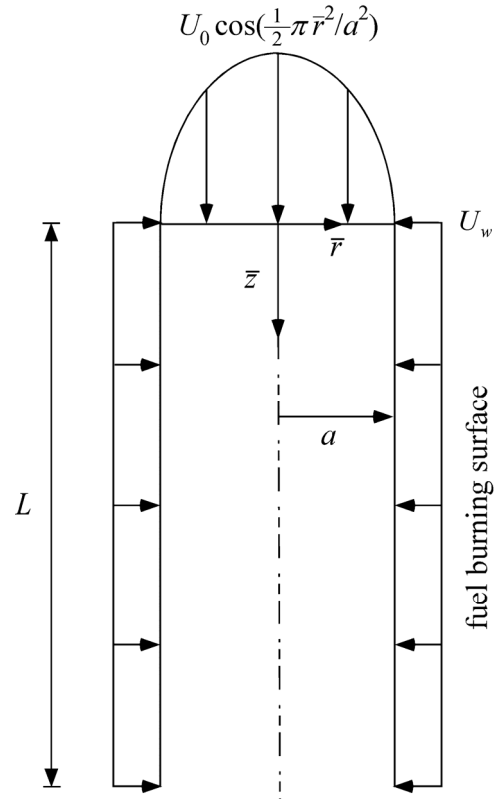


Fig. 3 Sketch of the rotational full-length hybrid model depicting mass addition along both sidewall and endwall boundaries. Here the oxidizer injection at the head end corresponds to a sinusoidal profile.

order using two head end injection profiles. These correspond to:

$$\bar{u}_z(\bar{r}, 0) = \begin{cases} U_0 \cos(\frac{1}{2} \pi \bar{r}^2 / a^2); & \text{harmonic} \\ U_0; & \text{uniform} \end{cases} \quad (1)$$

The main focus will be on the more realistic profile which will be used in conjunction with a rotational flow formulation that assumes normal sidewall mass addition.

A. Equations

A non-reactive flow can be considered, prompted by the weak reactions that accompany diffusion flames. Furthermore, the flow can be assumed to be (i) steady, (ii) inviscid, (iii) incompressible, (iv) rotational, and (v) axisymmetric. Based on these assumptions, Euler's equations become

$$\frac{1}{\bar{r}} \frac{\partial(\bar{r}\bar{u}_r)}{\partial\bar{r}} + \frac{\partial\bar{u}_z}{\partial\bar{z}} = 0 \quad (2)$$

$$\bar{u}_r \frac{\partial\bar{u}_r}{\partial\bar{r}} + \bar{u}_z \frac{\partial\bar{u}_r}{\partial\bar{z}} = -\frac{1}{\rho} \frac{\partial\bar{p}}{\partial\bar{r}} \quad (3)$$

$$\bar{u}_r \frac{\partial\bar{u}_z}{\partial\bar{r}} + \bar{u}_z \frac{\partial\bar{u}_z}{\partial\bar{z}} = -\frac{1}{\rho} \frac{\partial\bar{p}}{\partial\bar{z}} \quad (4)$$

B. Boundary Conditions

The boundary conditions are due to symmetry, no slip at the sidewall, and both head end and sidewall injection. Specifically, one can assume

- (a) uniform injection along the cylindrical sidewall
- (b) vanishing axial flow in fulfillment of the no slip boundary condition at the sidewall,
- (c) a prescribed injection pattern at the head end, and
- (d) axial symmetry about the centerline.

These particular conditions can be written as

$$\begin{cases} \bar{r} = a, 0 \leq \bar{z} < L, \bar{u}_r = -U_w \text{ (sidewall injection)} \\ \bar{r} = a, 0 \leq \bar{z} < L, \bar{u}_z = 0 \text{ (no slip at the wall)} \\ \bar{z} = 0, \forall \bar{r}, \bar{u}_z = U_0 \cos(\frac{1}{2} \pi \bar{r}^2 / a^2) \text{ (endwall)} \\ \bar{r} = 0, \forall \bar{z}, \bar{u}_r = 0 \text{ (axisymmetry)} \end{cases} \quad (5)$$

C. Normalization

In seeking a similarity solution, it is helpful to normalize all variables and operators. This can follow

$$z = \frac{\bar{z}}{a}; r = \frac{\bar{r}}{a}; \nabla = a\bar{\nabla}; p = \frac{\bar{p}}{\rho U_w^2} \quad (6)$$

$$u_r = \frac{\bar{u}_r}{U_w}; u_z = \frac{\bar{u}_z}{U_w}; u_0 = \frac{U_0}{U_w} \quad (7)$$

Here $U_0 = \bar{u}_z(0, 0)$ and $U_w = -\bar{u}_r(a, \bar{z})$ represent the maximum fluid injection velocity at the head end and the uniform wall injection velocity at the sidewall, respectively.

Pursuant to Eqs. (6)–(7), motion is prescribed become

$$\nabla \cdot \mathbf{u} = 0; \quad \mathbf{u} \cdot \nabla \mathbf{u} = -\nabla p \quad (8)$$

Using $\mathbf{u} \cdot \nabla \mathbf{u} = \frac{1}{2} \nabla(\mathbf{u} \cdot \mathbf{u}) - \mathbf{u} \times \nabla \times \mathbf{u}$ and taking the curl of the momentum equation, one obtains the steady and inviscid vorticity transport equation. This is

$$\nabla \times \mathbf{u} \times \boldsymbol{\Omega} = 0; \quad \boldsymbol{\Omega} \equiv \nabla \times \mathbf{u} \quad (9)$$

The corresponding boundary conditions reduce to

$$\begin{cases} u_r(1, z) = -1 \\ u_z(1, z) = 0 \\ u_z(r, 0) = u_0 \cos(\frac{1}{2} \pi r^2) \\ u_r(0, z) = 0 \end{cases} \quad (10)$$

Equation (9) must be solved in conjunction with the constraints granted by Eq. (10).

III. Rotational Solution

The current analysis focuses on the rotational solution corresponding to a sinusoidal head end injection velocity. To start, we consider the vorticity equation, namely,

$$\boldsymbol{\Omega} = \Omega_\theta \mathbf{e}_\theta = \left(\frac{\partial u_r}{\partial z} - \frac{\partial u_z}{\partial r} \right) \mathbf{e}_\theta \quad (11)$$

The vorticity stream function approach can be applied by introducing

$$u_r = -\frac{1}{r} \frac{\partial \psi}{\partial z}; \quad u_z = \frac{1}{r} \frac{\partial \psi}{\partial r} \quad (12)$$

Substitution into Eq. (9) yields

$$\frac{\partial(u_r \Omega_\theta)}{\partial r} + \frac{\partial(u_z \Omega_\theta)}{\partial z} = 0 \quad (13)$$

and so

$$\frac{\partial \psi}{\partial z} \frac{\partial}{\partial r} \left(\frac{\Omega_\theta}{r} \right) = \frac{\partial \psi}{\partial r} \frac{\partial}{\partial z} \left(\frac{\Omega_\theta}{r} \right) \quad (14)$$

This will be satisfied when

$$\frac{\Omega_\theta}{r} = F(\psi) \quad (15)$$

In seeking a closed-form solution, we choose

$$\Omega_\theta = C^2 r \psi \quad (16)$$

It must be borne in mind that this linear choice is not unique; other possible forms exist, including the case of $\Omega_\theta = C^2 = 0$ for which an irrotational solution is

realized. However, when Eq. (16) is inserted into the vorticity equation, one obtains the classic linear PDE

$$\frac{\partial^2 \psi}{\partial z^2} + \frac{\partial^2 \psi}{\partial r^2} - \frac{1}{r} \frac{\partial \psi}{\partial r} + C^2 \psi r^2 = 0 \quad (17)$$

At this point, three of the boundary conditions may be written for the stream function. Based on Eq. (10), one can write

$$\begin{cases} \frac{1}{r} \frac{\partial \psi(1, z)}{\partial z} = 1; & \frac{1}{r} \frac{\partial \psi(1, z)}{\partial r} = 0 \\ \frac{1}{r} \frac{\partial \psi(r, 0)}{\partial r} = u_0 \cos(\frac{1}{2} \pi r^2); & \frac{1}{r} \frac{\partial \psi(0, z)}{\partial z} = 0 \end{cases} \quad (18)$$

Using separation of variables, one sets

$$\psi(r, z) = f(r)g(z) \quad (19)$$

This reduces Eq. (17) into

$$-\frac{g''}{g} = \frac{f''}{f} - \frac{1}{r} \frac{f'}{f} + C^2 r^2 = \pm \lambda^2 \quad (20)$$

The only feasible case for the problem at hand corresponds to $\lambda = 0$. At the outset, one collects

$$g(z) = C_1 z + C_2 \quad (21)$$

and

$$f'' - \frac{1}{r} f' + C^2 r^2 f = 0 \quad (22)$$

The latter can be rearranged into

$$\frac{1}{r} \frac{d}{dr} \left(\frac{1}{r} \frac{df}{dr} \right) + C^2 f = 0 \quad (23)$$

Using the transformation, $\eta = \frac{1}{2} r^2$, one finds

$$\frac{d}{d\eta} \left(\frac{df}{d\eta} \right) + C^2 f = 0 \quad (24)$$

hence

$$f(\eta) = A \cos(C\eta) + B \sin(C\eta) \quad (25)$$

or

$$f(r) = A \cos(\frac{1}{2} Cr^2) + B \sin(\frac{1}{2} Cr^2) \quad (26)$$

The stream function becomes

$$\psi = (C_1 z + C_2) [A \cos(\frac{1}{2} Cr^2) + B \sin(\frac{1}{2} Cr^2)] \quad (27)$$

This, in turn, unravels

$$u_z = (C_1 z + C_2) \left[-A C \sin(\frac{1}{2} Cr^2) + B C \cos(\frac{1}{2} Cr^2) \right] \quad (28)$$

and

$$u_r = -\frac{C_1}{r} \left[-A \cos(\frac{1}{2} Cr^2) + B \sin(\frac{1}{2} Cr^2) \right] \quad (29)$$

From $u_r(0, z) = 0$, one finds, $A = 0$. Hence,

$$u_z = (C_1 z + C_2) \left[B C \cos(\frac{1}{2} Cr^2) \right] \quad (30)$$

and

$$u_r = -C_1 \left[B \sin(\frac{1}{2} Cr^2) \right] / r \quad (31)$$

Then, based on $u_z(1, z) = 0$ one gets $\sin(\frac{1}{2} C) = 0$ or $C = \pi$. At the outset, one collects

$$\begin{cases} u_z = (C_1 z + C_2) \left[B \pi \cos(\frac{1}{2} \pi r^2) \right] \\ u_r = -C_1 B \sin(\frac{1}{2} \pi r^2) / r \end{cases} \quad (32)$$

The key boundary condition at the head end, which permits the introduction of a secondary stream, may now be applied. By putting

$$u_z(r, 0) = u_0 \cos(\frac{1}{2} \pi r^2) \quad (33)$$

one deduces $u_0 = C_2 B \pi$; the last constant can be obtained by writing

$$u_z = (C_1 B \pi z + u_0) \left[\cos(\frac{1}{2} \pi r^2) \right] \quad (34)$$

and imposing $u_r(1, z) = -1$. One reaps $C_1 = B^{-1}$. The solution we seek can finally be expressed as

$$\psi = (z + u_0 / \pi) \sin(\frac{1}{2} \pi r^2) = (z + u_h) \sin(\frac{1}{2} \pi r^2) \quad (35)$$

As shown in Fig. 4, increasing the head end wall injection parameter increases the flow turning severity near the sidewall. Specifically, as u_h is increased from 50 to 200, the streamlines, which otherwise resemble those of an SRM, become dominated by axial (parallel-flow) motion everywhere except in the neighborhood of the sidewall. This can be clearly attributed to the increased propensity of the axial stream bursting into the chamber from the head end. At larger u_h the normally injected stream is met by an overwhelmingly larger axial flow that forces it to turn and merge in the downstream direction. In practice, the values of U_0 and U_w could be calibrated to reproduce the patterns associated with a prototypical hybrid engine.

Based on Eq. (35) other pertinent variables may be evaluated. For example, one finds

$$u_r = -\frac{1}{r} \sin(\frac{1}{2} \pi r^2) \quad (36)$$

$$u_z = \pi(z + u_h) \cos(\frac{1}{2} \pi r^2) \quad (37)$$

$$\Omega_\theta = \pi^2(z + u_h) r \sin(\frac{1}{2} \pi r^2) \quad (38)$$

$$\frac{\partial p}{\partial r} = -\frac{-1 + \pi r^2 \sin(\pi r^2) + \cos(\pi r^2)}{2r^3} \quad (39)$$

$$\frac{\partial p}{\partial z} = -\pi^2(u_h + z) \quad (40)$$

and, the pressure drop from the head end, namely,

$$\Delta p = \frac{-1 - 2\pi^2 r^2 z(2u_h + z) + \cos(\pi r^2)}{4r^2} \quad (41)$$

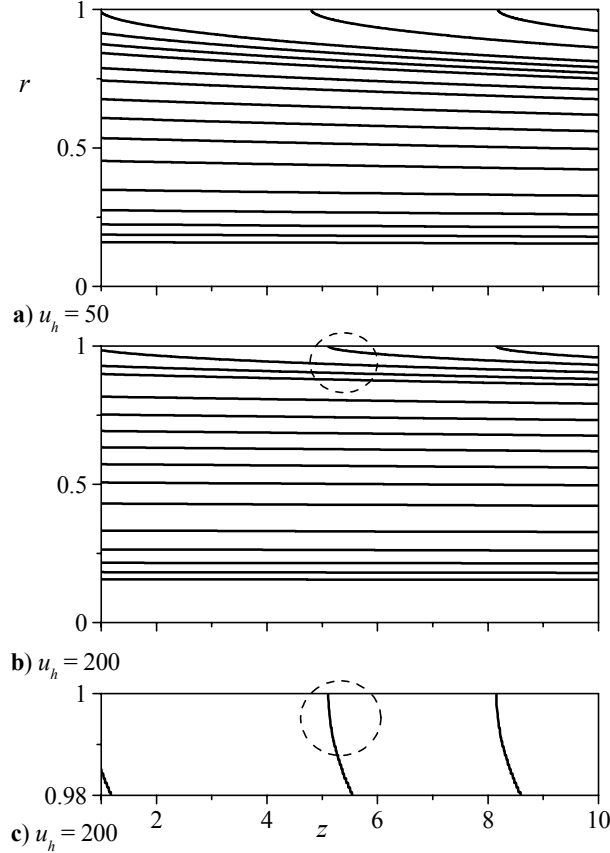


Fig. 4 Rotational streamlines shown for two increasing head end injection parameters. The inset in part c) corresponds to a magnified section of part b) illustrating the normal sidewall injection feature.

In Fig. 5, the two velocity components, vorticity and the radial pressure drop at the head end are plotted. While the axial velocity increases linearly with the head end injection parameter, the radial velocity remains unaffected. In fact, the radial component is seen to be identical to its counterpart in SRMs, namely, that of Culick.¹ In Fig. 5c, the vorticity is seen to be largest near the sidewall where flow is entering perpendicularly to the fuel surface. Away from the wall, vorticity decays rapidly; it approaches zero near the centerline where the flow becomes nearly uniform. As for the pressure drop, Fig. 5d illustrates how $\Delta p(r, 0)$ in the head end plane can surpass its wall value when

$$\frac{1}{2}\sqrt{2} < r < 1 \quad (42)$$

In this range, the largest magnitude corresponds to $\Delta p = -0.569108$. This extremum can be obtained by differentiating Eq. (41) at fixed z . Thus, by letting

$$\frac{-1 + \pi r_m^2 \sin(\pi r_m^2) + \cos(\pi r_m^2)}{2r_m^3} = 0 \quad (43)$$

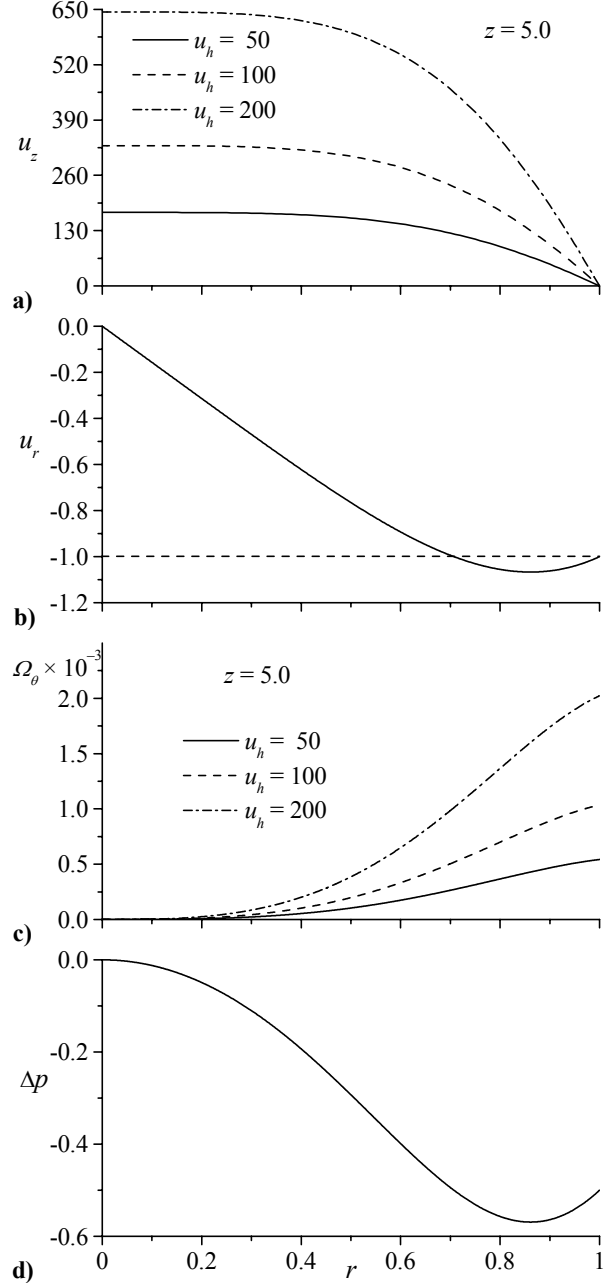


Fig. 5 Description of a) axial and b) radial velocities in addition to c) vorticity and d) pressure drop at the chamber's head end. Both axial velocity and vorticity are shown at a fixed axial position.

one may expand the numerator using a Taylor series about $\frac{1}{2}\sqrt{3}$; forthwith, a quadratic equation of the form $ax^2 + bx + c = 0$ is obtained where

$$\begin{cases} ax^2 = -72\pi^2\sqrt{2}r_m^2 - 36\pi^3\sqrt{2}r_m^2 \\ bx = 48\pi^2\sqrt{6}r_m + 36\pi^3\sqrt{6}r_m \\ c = -64 - 32\sqrt{2} + 24\pi\sqrt{2} - 18\pi^2\sqrt{2} - 27\pi^3\sqrt{2} \end{cases} \quad (44)$$

The extrema of Δp correspond to the two possible roots, one of which being $r_m = 0.861405$. Note that the radial pressure variation is strongly connected with the radial velocity shown in Fig. 5b; both experience an unexpected surge in magnitude immediately after injection (thus exceeding their absolute value at the wall). This behavior is due to the decrease in area open to radial flow near $r = 1$.

IV. Irrotational Solution

The same analysis can be repeated assuming a uniform velocity profile at the head end (see Fig. 6). To permit an exact derivation, the flow must be irrotational and, by the same token, the condition of normal sidewall injection must be relaxed. The ensuing analysis is fairly straightforward; its three needed conditions are

$$u_r(1, z) = -1; \quad u_z(r, 0) = u_0 = 2u_h; \quad u_r(0, z) = 0 \quad (45)$$

Using $C^2 = 0$ in Eq. (17), one recovers the potential flow solution expressed by

$$\psi = (z + u_h) r^2 \quad (46)$$

$$u_r = -r \quad (47)$$

$$u_z = 2(z + u_h) \quad (48)$$

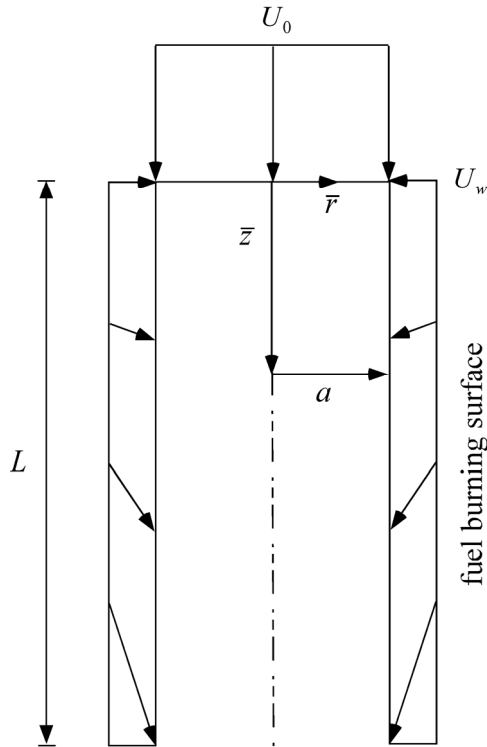


Fig. 6 Sketch of the irrotational hybrid model depicting uniform mass injection at the head end and slip along the sidewall.

$$\Omega_\theta = 0 \quad (49)$$

$$\frac{\partial p}{\partial r} = -r \quad (50)$$

$$\frac{\partial p}{\partial z} = -4(u_h + z) \quad (51)$$

and, the pressure drop along the chamber length,

$$\Delta p = -\frac{1}{2}r^2 - 4\left(u_h z + \frac{1}{2}z^2\right) \quad (52)$$

This concludes our presentation of the two basic solutions appropriate for internal flow modeling of classic hybrid motors.

V. Concluding Remarks

In this study, a rotational model is presented as a means to describe the gas dynamics in a full-length hybrid motor with circular bore. Our idealization is based on inviscid, rotational and incompressible motion in conjunction with a harmonic injection profile at the chamber head end. The mean flow emerging from sidewall and endwall mass addition is rotational and satisfies the no slip condition at the wall. Another mean flow model that permits uniform injection at the head end is presented as a feasible alternative, albeit irrotational. The two solutions may be helpful to point out, especially that their parameters, U_0 and U_w , can be potentially adjusted to mimic the bulk gas motion reported in classic hybrid geometry. Finally, it should be noted that a higher order viscous formulation is possible using asymptotic tools. This solution can be obtained by perturbing the regularized governing equation using the reciprocal of the injection Reynolds number, Re . The resulting solution can be developed, albeit more complex and, perhaps, less portable.

Acknowledgments

This project was sponsored by the Faculty Early Career Development (CAREER) Program of the National Science Foundation under Grant No. CMS-0353518. The authors sincerely appreciate the valuable support received from Dr. Masayoshi Tomizuka, Program Director, Dynamic Systems and Control.

References

- ¹Culick, F. E. C., "Rotational Axisymmetric Mean Flow and Damping of Acoustic Waves in a Solid Propellant Rocket," *AIAA Journal*, Vol. 4, No. 8, 1966, pp. 1462-1464.
- ²Taylor, G. I., "Fluid Flow in Regions Bounded by Porous Surfaces," *Proceedings of the Royal Society, London, Series A*, Vol. 234, No. 1199, 1956, pp. 456-475.

- ³Baum, J. D., Levine, J. N., and Lovine, R. L., "Pulsed Instabilities in Rocket Motors: A Comparison between Predictions and Experiments," *Journal of Propulsion and Power*, Vol. 4, No. 4, 1988, pp. 308-316.
- ⁴Sabnis, J. S., Gibeling, H. J., and McDonald, H., "Navier-Stokes Analysis of Solid Propellant Rocket Motor Internal Flows," *Journal of Propulsion and Power*, Vol. 5, No. 6, 1989, pp. 657-664.
- ⁵Dunlap, R., Willoughby, P. G., and Hermsen, R. W., "Flowfield in the Combustion Chamber of a Solid Propellant Rocket Motor," *AIAA Journal*, Vol. 12, No. 10, 1974, pp. 1440-1445.
- ⁶Dunlap, R., Blackner, A. M., Waugh, R. C., Brown, R. S., and Willoughby, P. G., "Internal Flow Field Studies in a Simulated Cylindrical Port Rocket Chamber," *Journal of Propulsion and Power*, Vol. 6, No. 6, 1990, pp. 690-704.
- ⁷Yamada, K., Goto, M., and Ishikawa, N., "Simulative Study of the Erosive Burning of Solid Rocket Motors," *AIAA Journal*, Vol. 14, No. 9, 1976, pp. 1170-1176.
- ⁸Majdalani, J., Vyas, A. B., and Flandro, G. A., "Higher Mean-Flow Approximation for a Solid Rocket Motor with Radially Regressing Walls," *AIAA Journal*, Vol. 40, No. 9, 2002, pp. 1780-1788.
- ⁹Zhou, C., and Majdalani, J., "Inner and Outer Solutions for the Injection Driven Channel Flow with Retractable Walls," AIAA Paper 2003-3728, June 2003.
- ¹⁰Zhou, C., and Majdalani, J., "Improved Mean Flow Solution for Slab Rocket Motors with Regressing Walls," *Journal of Propulsion and Power*, Vol. 18, No. 3, 2002, pp. 703-711.
- ¹¹Chiaverini, M. J., Johnson, D. K., Serin, N., Lu, Y. C., Kuo, K. K., and Risha, G. A., "Regression Rate Behavior of Hybrid Rocket Solid Fuels," *Journal of Propulsion and Power*, Vol. 16, No. 1, 2000, pp. 125-132.
- ¹²Chiaverini, M. J., Kuo, K. K., Peretz, A., and Harting, G. C., "Regression Rate and Heat Transfer Correlations for Hybrid Rocket Combustion," *Journal of Propulsion and Power*, Vol. 17, No. 1, 2001, pp. 99-110.
- ¹³Jenkins, R. M., and Cook, J. R., "A Preliminary Analysis of Low Frequency Pressure Oscillations in Hybrid Rocket Motors," 31st AIAA/ASME/SAE/ASEE Joint Propulsion Conference Paper 95-2690, July 10-12 1995.
- ¹⁴Krier, H., and Kerzner, H., "An Analysis of the Chemically Reacting Boundary Layer During Hybrid Combustion," AIAA/SAE 8th Joint Propulsion Specialist Conference Paper 72-1144, November 29-December 1 1972.
- ¹⁵Knuth, W. H., Chiaverini, M. J., Sauer, J. A., and Gramer, D. J., "Solid-Fuel Regression Rate Behavior of Vortex Hybrid Rocket Engines," *Journal of Propulsion and Power*, Vol. 18, No. 3, 2002, pp. 600-609.
- ¹⁶Karabeyoglu, M. A., Altman, D., and Cantwell, B. J., "Combustion of Liquifying Hybrid Propellants: Part 1, General Theory," *Journal of Propulsion and Power*, Vol. 18, No. 3, 2002, pp. 610-620.
- ¹⁷Karabeyoglu, M. A., and Cantwell, B. J., "Combustion of Liquifying Hybrid Propellants: Part 2, Stability of Liquid Films," *Journal of Propulsion and Power*, Vol. 18, No. 3, 2002, pp. 621-630.